CIRP Annals - Manufacturing Technology 73 (2024) 321–324

Contents lists available at ScienceDirect

CIRP Annals - Manufacturing Technology

journal homepage: https://www.editorialmanager.com/CIRP/default.aspx

Feedforward compensation of the pose-dependent vibration of a silicon wafer handling robot

Cheng-Hao Chou, Chen Qian, Yung-Chun Lin, Shorya Awtar, Chinedum E. Okwudire (2)*

Department of Mechanical Engineering, University of Michigan, Ann Arbor, USA

ARTICLE INFO

Article history:
Available online 22 May 2024

Keywords:
Robot
Modelling
Control

ABSTRACT

Frog-legged robots are commonly used for silicon wafer handling in semiconductor manufacturing. However, their precision, speed and versatility are limited by vibration which varies with their position in the workspace. This paper proposes a methodology for modelling the pose-dependent vibration of a frog-legged robot as a function of its changing inertia, and its experimentally-identified joint stiffness and damping. The model is used to design a feedforward tracking controller for compensating the pose-dependent vibration of the robot. In experiments, the proposed method yields 65–73% reduction in RMS tracking error compared to a baseline controller designed for specific poses of the robot.

1. Introduction

Semiconductor manufacturing involves numerous steps that must be executed with precision to achieve increasingly stringent quality specifications for electronic devices [1–3]. Simultaneously, the industry faces increasing pressures for higher throughput and flexibility to address rapidly growing and changing demands for electronics [4].

Wafer handling robots are used extensively for moving silicon wafers through various steps in the semiconductor manufacturing process [5,6]. Therefore, their precision, speed, and versatility are critical to achieving the quality, throughput and flexibility needs of the industry. In practice, there are two types of wafer handling robots, one which utilizes a parallel structure, and another that adopts a serial robot arm structure. In this work, a wafer handling robot with parallel structure, referred to as a frog-legged robot, is studied. The main advantage of a frog-legged robot is its simple design [7], ability to manipulate large load and enhanced rigidity due to the closed loop mechanism [8].

Fig. 1 shows the top view and section views of the specific architecture of frog-legged robots used in this study. The left and right linkages of the frog legs are driven by separate motors (Motor 1 and Motor 2, respectively). However, the motor torques are transmitted indirectly to the linkages through belts and a magnetic coupling. The magnetic coupling consists of sixteen attracting magnet pole pairs that are mounted on the outer and inner magnet retainers (see Fig. 1(c)). In this way, it provides a low-cost, contactless transmission of motion between the inner processing chamber which lies at atmospheric pressure and the outer chamber which lies in a vacuum. This prevents contaminants, like dust and lubricating oil, emanating from the motors from reaching the vacuum chamber. It also prevents corrosive chemicals from the processing in the vacuum chamber from harming the motors [9,10]. However, due to the low stiffness of the magnetic coupling, the robot is prone to vibration. Excessive vibration could lead to slippage of the silicon wafer on the blade (i.e., the end effector that carries the wafer) or collision of the wafer with objects within the processing chamber, leading to damage of the wafer. Therefore, it is important to mitigate vibration in order to accurately track the motions of the robot at high speed. However, a major problem with the robot's vibration is that it is pose-dependent, meaning that the vibration behaviour (e.g., natural frequency) changes as the robot moves from position to position within its workspace.

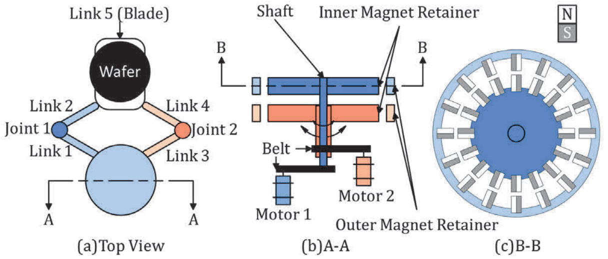

Fig. 1. Schematic diagram of (a) top view of the robot (b) vertical section view, and (c) horizontal section view of the interior of the robot.

There is some work in the literature on compensating the vibration of frog-legged robots. For example, Wang et al. [11] used an active vibration rejection method via vibrotactile transducers for vibration reduction. However, this method requires an additional actuator and sensor located at the blade in vacuum, which is costly. A promising approach for compensating vibration is using feedforward control, realized by modifying the trajectory sent to the vibrating machine. It has been used extensively for machine tools and robots [12–16]. For example, Yu et al. [13] implemented model-based torque feedforward control in addition to a basic tri-loop PID controller on a frog-legged robot. However, they did not address the pose-dependent vibration behaviour, which may limit the effectiveness of the controller. To the author's best knowledge, there is no existing work in the open literature addressing the pose-dependent vibration of frog-legged robots.

To tackle this shortcoming, this paper proposes a methodology for modelling the pose-dependent dynamics of a frog-legged robot as a function of its changing inertia, and experimentally identified joint stiffness

---

* Corresponding author.
E-mail address: okwudire@umich.edu (C.E. Okwudire).

https://doi.org/10.1016/j.cirp.2024.04.081

and damping. The model is then used to design a pose-dependent filtered B-spline (FBS) tracking controller [15,17] for compensating the pose-dependent vibration of the robot. Note that in [17], the delta robot that was studied could be decoupled into two sub-models and the rotational inertia could be ignored, which simplified the modelling of its pose-dependent dynamics. Conversely, the frog-legged robot has non-negligible rotational inertia and fully coupled dynamics. Thus, a different method for modelling its pose-dependent dynamics is needed.

The outline of this paper is as follows: In Section 2, the analytical modelling of the pose-dependent dynamics is presented. In Section 3, the obtained model is integrated with a time-varying FBS controller. The experimental validation of the proposed method on the tracking of the frog-legged robot is presented in Section 4, followed by conclusions and future work in Section 5.

2. Modelling of pose-dependent dynamics

The blade (end effector) of the frog legged robot has two directions of motion: radial (r) and rotational (θ), as depicted in Fig. 2. The r motion is produced by rotating the motors in opposite directions, while the θ motion is produced by rotating them in the same direction. The r direction is more susceptible than θ to pose-dependent dynamics. This is because the dynamics of the robot only change when the blade position varies in the r direction, and in normal operation only one direction is commanded at a time. Accordingly, r vibration dynamics change during motions in the r direction, while θ vibration dynamics are constant during θ motions. Hence, our pose-dependent modelling and control efforts in this paper will focus on the r direction.

Fig. 2 shows our modelling and control strategy. The magnetic coupling is treated as a torsional spring and damper between the rotations of the inner and outer magnet retainers, while the links are treated as rigid bodies with both translational and rotational inertia. The stiffness and damping coefficients are assumed to be constants while the effective inertia varies with pose. The stiffness and damping coefficients are identified from a few frequency response function (FRF) measurements from the robot, and are combined with the computed pose-dependent inertia matrix to determine the robot dynamics at any arbitrary position of the end effector. The pose-dependent dynamics can then be used for feedforward (FF) control.

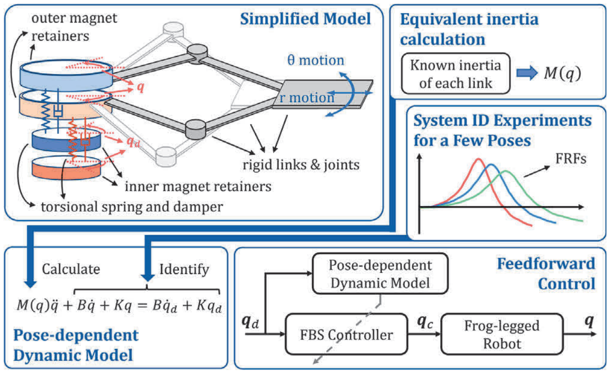

Fig. 2. Overview of the proposed modelling and control strategy.

Mathematically, the model is described by the rigid-body dynamic equation of motion with joint flexibility, i.e.,

$$\mathbf{M}(\boldsymbol{q})\ddot{\boldsymbol{q}} = \mathbf{K}(\boldsymbol{q}_d - \boldsymbol{q}) + \mathbf{B}(\dot{\boldsymbol{q}}_d - \dot{\boldsymbol{q}}) \tag{1}$$

where $\boldsymbol{q}_d$ and $\boldsymbol{q}$ are respectively the rotating angles of the two motors and the two outer magnet retainers, $\mathbf{M}(\boldsymbol{q})$ is the inertia matrix of the system, and $\mathbf{K}$ and $\mathbf{B}$ are the diagonal stiffness and damping matrices of the magnetic coupling. Note that the Coriolis $\mathbf{C}(\boldsymbol{q}, \dot{\boldsymbol{q}})$ and the gravity $\mathbf{G}(\boldsymbol{q})$ terms, which exist in robot multi-body dynamics, are omitted from Eq. (1) due to their negligible effects on vibration. The pose-dependent vibration dynamics are mainly governed by the inertia matrix $\mathbf{M}(\boldsymbol{q})$, which is computed as

$$\mathbf{M}(\boldsymbol{q}) = \sum_{i=1}^{5} \boldsymbol{J}_i^T(\boldsymbol{q}) \begin{bmatrix} m_i & 0 & 0 \\ 0 & m_i & 0 \\ 0 & 0 & I_i \end{bmatrix} \boldsymbol{J}_i(\boldsymbol{q}) \tag{2}$$

where m_i, I_i, and $\boldsymbol{J}_i$ denote the translational inertia, rotational inertia, and the Jacobian about the reference point of each link.

To facilitate the analysis of the r direction motion, Eq. (1) is further rewritten to explicitly describe r and θ motion by applying the following transformation:

$$\bar{\boldsymbol{q}} = \begin{bmatrix} q_r \\ q_\theta \end{bmatrix} = \mathbf{T}\boldsymbol{q} \tag{3}$$

where $\mathbf{T}$ is a transformation matrix. Accordingly, the equation of motion becomes

$$\overline{\mathbf{M}}(\boldsymbol{q})\ddot{\bar{\boldsymbol{q}}} = \overline{\mathbf{K}}(\bar{\boldsymbol{q}}_d - \bar{\boldsymbol{q}}) + \overline{\mathbf{B}}(\dot{\bar{\boldsymbol{q}}}_d - \dot{\bar{\boldsymbol{q}}}) \tag{4}$$

where $\overline{\mathbf{M}}(\boldsymbol{q}) = \mathbf{T}\mathbf{M}(\boldsymbol{q})\mathbf{T}^{-1}$, $\overline{\mathbf{K}} = \mathbf{T}\mathbf{K}\mathbf{T}^{-1}$, and $\overline{\mathbf{B}} = \mathbf{T}\mathbf{B}\mathbf{T}^{-1}$. It is notable that due to the symmetric structure of the frog-legged robot investigated in this paper, the resulting $\overline{\mathbf{M}}$, $\overline{\mathbf{K}}$ and $\overline{\mathbf{B}}$ are diagonally dominant. Therefore, the r and θ directions can be decoupled, and the r vibration dynamics can be extracted as

$$M_r(q_r)\ddot{q}_r + B_r\dot{q}_r + K_r q_r = B_r\dot{q}_{r,d} + K_r q_{r,d} \tag{5}$$

where M_r, B_r, and K_r are the first-row and first-column elements of $\overline{\mathbf{M}}$, $\overline{\mathbf{B}}$, and $\overline{\mathbf{K}}$. After Eq. (5), along with the value of $M_r(q_r)$, is derived, a few system identification experiments are performed to generate the FRFs for 3 different blade positions (i.e., with the blade at both extremes and at the middle of its travel range). Then, with the assumption that the FRF's peak frequency is equal to its natural frequency, the stiffness and damping coefficients of each individual system identification experiment are obtained as

$$K_{r,j} = M_{r,j}\omega_{pk,j}^2, B_{r,j} = M_{r,j}\omega_{pk,j}\sqrt{\frac{1}{M_{pk,j}^2 - 1}} \tag{6}$$

where $\omega_{pk,j}$ and $M_{pk,j}$ are the natural frequency and the magnitude of the j-th FRF measurement (j = 1,2,3). These results are then averaged to give the final values of K_r and B_r as in Eq. (5).

3. Pose-dependent feedforward controller design

Once the modelling of the handling robot is completed using the method proposed in Section 2, the linear parameter-varying dynamics dependent on the blade position, denoted as $G(q_r)$, can be obtained and used for FF compensation. The FF controller used in this study is the linear time varying (LTV) FBS controller similar to the one in [17].

The FBS controller [15] formulates the input command $\boldsymbol{q}_{r,c}$ as a linear combination of a set of B-spline basis functions $\boldsymbol{\psi}_n$ with unknown coefficients $\boldsymbol{\gamma}$, i.e.,

$$\boldsymbol{q}_{r,c} = \sum_n \boldsymbol{\psi}_n\gamma_n = \Psi\boldsymbol{\gamma} \tag{7}$$

The basis functions $\boldsymbol{\psi}_n$ are then filtered using the system's dynamics G to become $\sim\boldsymbol{\psi}_n$, thereby giving the output prediction as $\hat{\boldsymbol{q}}_r = \sum_n \sim\boldsymbol{\psi}_n\gamma_n = \sim\Psi\boldsymbol{\gamma}$, and lastly the optimal coefficients $\boldsymbol{\gamma}^*$ are selected by minimizing the tracking error $\boldsymbol{e}$ between the desired trajectory $(\boldsymbol{q}_{r,d})$ and the output prediction $(\hat{\boldsymbol{q}}_r)$, $\boldsymbol{e} = \boldsymbol{q}_{r,d} - \hat{\boldsymbol{q}}_r$, i.e.,

$$\boldsymbol{\gamma}^* = \underset{\boldsymbol{\gamma}}{\operatorname{argmin}} \parallel \boldsymbol{q}_{r,d} - \sim\Psi\boldsymbol{\gamma} \parallel = \left(\sim\Psi^T \sim\Psi\right)^{-1} \sim\Psi^T\boldsymbol{q}_{r,d} \tag{8}$$

In the standard FBS for LTI systems, $\sim\boldsymbol{\psi}_n$ can be obtained simply by passing $\boldsymbol{\psi}_n$ though a fixed transfer function G. However, for LTV systems, the output position needs to be known at every timestep to determine the time-varying dynamics, making Eq. (8) inapplicable and the overall optimization process iterative. To simplify this, the position $\boldsymbol{q}_r$ used for determining the dynamics is approximated by the desired position $\boldsymbol{q}_{r,d}$ at each timestep. In other words, the system dynamics at each timestep is determined by $\boldsymbol{q}_{r,d}$ at the corresponding timestep and can be expressed by

$$G(q_{r,d}) = \frac{Q_r(s)}{Q_{r,d}(s)} = \frac{B_r s + K_r}{M_r(q_{r,d})s^2 + B_r s + K_r} \tag{9}$$

The transfer function in Eq. (9) is further converted to a discrete infinite impulse response (IIR) filter as

$$G_{IIR} = \frac{b_{-1}z^{-1} + b_{-2}z^{-2}}{1 + a_{-1}z^{-1} + a_{-2}z^{-2}} \tag{10}$$

where z is the forward shift operator. The a and b terms are functions of time. Each row of Ψ is iteratively filtered through G_{IIR} based on the corresponding dynamics by only one timestep to construct $\sim\Psi$. Once $\sim\Psi$ is established, Eqs. (7) and (8) are applied to compute the optimal command as in standard FBS [15].

4. Experimental validation on silicon wafer handling robot

4.1. Experimental setup

The experimental setup in this study consists of the frog-legged robot, two motor drivers, a motor controller, a distance sensor, a data logger, an accelerometer, and a host PC. The layout of the overall experimental setup is as shown in Fig. 3.

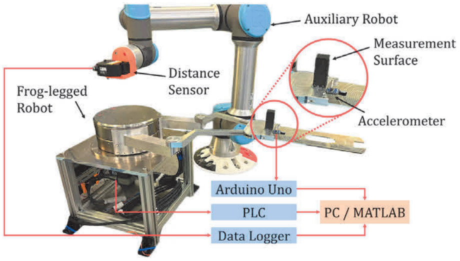

Fig. 3. Experimental setup for controlling the frog-legged robot.

The stepper motors are each driven by a motor driver integrated with a programmable logic controller (PLC). The PLC communicates with a host PC via EtherCAT, enabling high-speed communication for real-time control. This structure allows precise and synchronized control of the frog-legged robot using an ethernet cable connected to a PC. An accelerometer (ADXL 345) mounted on the blade and a distance sensor (mounted on an auxiliary robot arm) were used to quantify the amount of vibration when the robot operates. To measure the vibration in the r direction, a 3D printed block with negligible mass was attached on the blade as a measurement surface to serve as a measurement target for the distance sensor. A data logger for the distance sensor received the position data and stored it on the host PC. The accelerometer was programmed to measure the frequency response of the robot in the r direction, which was used to construct the pose-dependent model in Section 4.2, as well as to validate the vibration compensation performance in Section 4.3.

4.2. Validation of modelling of pose-dependent dynamics

The ability of the proposed modelling method to capture the pose-dependent dynamics is presented in this section. To compute the equivalent inertia, which dominates the robot dynamics, the translational and rotational inertia as well as the reference point (typically center of mass) of each link is required. The masses and inertias of the links were obtained from computer aided design (CAD) models of the robot or via measurements, and then used to compute the equivalent inertia matrix $M_r(q_r)$ using Eq. (2).

After the equivalent inertia values were computed, system identification experiments using sine sweep commands at three selected blade locations, $q_r = 220$ (nearest), $q_r = 400$ (middle), and $q_r = 580$ (farthest) mm, were performed to generate the FRFs and identify the stiffness and damping coefficients. These three sets of coefficients were then averaged to yield the K_r and B_r constants used in Eq. (9) to generate the system's dynamics. Table 1 summarizes the inertia, stiffness, and damping values identified.

Table 1
Inertia, stiffness, and damping values of each link. The numbering of the links is shown in Fig. 1. Note that links 1′s and 3′s rotational inertia are based on the center of the magnet coupling while the rest are based on their center of mass. Also, the values of the corresponding symmetric component may have slight deviation.

Inertia of	Links 1 & 3	Links 2 & 4	Link 5 (blade)
Translational inertia [kg]	2.35	0.15	0.17
Rotational inertia [g·m^2]	17.97	0.74	0.94
Stiffness and Damping of Magnet Coupling			
Stiffness coefficient [Nm/rad]	153		
Damping coefficient [Nm-s/rad]	1.12		

Fig. 4 shows the resonance frequencies at 19 selected poses measured from experiments and predicted by the proposed modelling method. The 19 poses range from $q_r = 220$ mm to $q_r = 580$ mm at increments of 20 mm. The proposed model captures the resonance frequencies accurately based on only three system identification experiments at the locations marked in the figure. However, deviations between measurement and prediction are also observed at poses that are close to the nearest or farthest blade position. Possible reasons for the deviations include the averaging of identified parameters, the effect of approximations, and unmodeled dynamics (e.g., the stiffness and damping of other joints) which are amplified at the extremes of the motion range. Moreover, the stiffness of the magnetic coupling is amplitude dependent [18]. Therefore, changes in pose (which may lead to changes in vibration amplitudes) could affect the stiffness values.

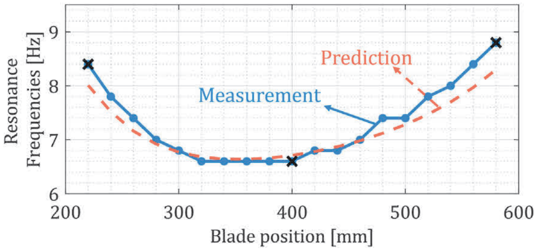

Fig. 4. Comparison of the resonance frequencies (here defined as the frequencies where the FRF magnitude is the largest) from measured FRFs and the proposed model derived from the poses indicated by crosses (×).

4.3. Validation of the proposed controller

The performance of the proposed modelling method applied to feedforward control is validated in this section. The pose-dependent dynamics derived from Section 4.2 are incorporated into the LTV FBS controller presented in Section 3 to track point-to-point motions of the frog-legged robot. The tracking performance of the LTV FBS controller are compared with the uncompensated case and three LTI FBS controllers that use the dynamics measured at $q_r = 220$, $q_r = 400$, and $q_r = 580$ mm. Multiple trajectories with different starting and ending positions, but with the same velocity, acceleration, and jerk constraints of

$$F_{max} = 200\ \text{mm/s}, A_{max} = 3\ \text{m/s}^2, \text{and}\ J_{max} = 100\ \text{m/s}^3 \tag{11}$$

are presented. Specifically, the results of the extension and retraction motions of the full range case (220 to 580 mm), half range cases (220 to 400 mm and 400 to 580 mm), and an arbitrary range case (300 to 500 mm), are discussed to show the advantage of the LTV FBS controller. By demonstrating that the proposed method can improve the tracking performance at any position, the versatility of the frog-legged robot can thereby be enhanced.

Fig. 5(a)-(c) show the acceleration and position respectively measured from the accelerometer and the laser scanner for each case studied. Note that due to its limited measurement range, only the position measurements at the end of each motion are captured by the laser scanner. Observe from the position measurements that the uncompensated cases always have significant overshoot and vibration. The LTI FBS controllers demonstrate very accurate reference tracking when the model used for the controller matches the end position of the trajectory. However, the LTV FBS controller exhibits accurate tracking for all cases. It is notable that the LTI FBS controller based on the 220 mm dynamics also performs well at 580 mm blade location, so does LTI FBS with 400 mm dynamics at 300 mm blade location. This is because the dynamics at both locations are similar, as also seen from Fig. 4. The vibration-induced errors for all cases studied are summarized in Table 2. The LTV FBS controller yields between 65% and 73% reduction in average RMS error compared to the LTI FBS controllers.

The acceleration measurements in Fig. 5 give similar conclusions as the position measurements. At the end of the motion, significant residual vibration is observed for the uncompensated case, which is efficiently mitigated by the proposed LTV FBS controller and by the LTI FBS controllers if the dynamics used are carefully chosen. However, some vibrations still exist during the start of the motion due to modelling inaccuracy and the approximations inherent in performing FF control using FBS. During the same portion, it is also found that the oscillation of LTI FBS with 400 mm dynamics is always lowest. This may be because the natural frequency at $q_r = 400$ mm is low, and thus the FF controller attenuates lower-frequency signal, of which the point-to-point motion mostly is composed. This, however, does not infer better tracking.

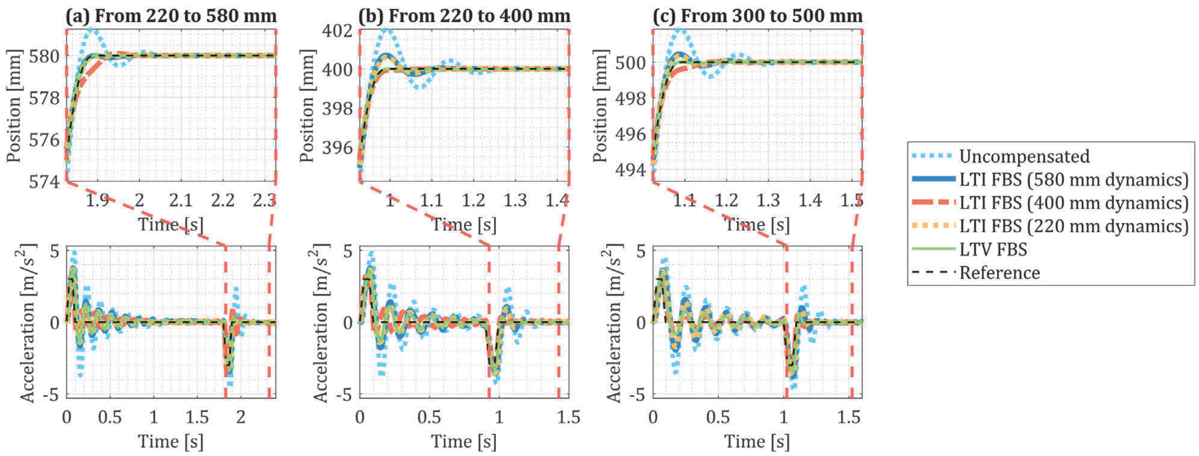

Fig. 5. Vibration compensation performance of the LTV FBS controller with the proposed model compared to other controllers for point-to-point extension motion between (a) 220 – 580, (b) 220 – 400, and (c) 300 – 500 mm blade position.

Table 2
Summary of the RMS vibration-induced position errors at the ending position of all cases (Unit: μm).

Trajectory		LTV FBS	LTI FBS (220 mm)	LTI FBS (400 mm)	LTI FBS (580 mm)	uncompen-sated
extension	220–400 mm	40.4	192.4	36.6	226.2	690.4
	220–580 mm	30.8	41.6	217.5	50.3	410.8
	400–580 mm	42.7	47.2	214.6	62.2	434.2
	300–500 mm	48.6	132.1	129.8	162.4	626.3
retraction	220–400 mm	25.3	36.2	213.0	47.8	465.7
	220–580 mm	32.3	36.1	178.1	82.6	479.6
	400–580 mm	27.2	139.9	43.7	182.4	627.4
	300–500 mm	42.6	191.4	45.1	256.2	665.0
Average RMS error		36.2	102.1	134.8	133.8	549.9

5. Conclusion and future work

This paper proposes an efficient modelling technique for the pose-dependent dynamics of a frog-legged silicon wafer handling robot. The proposed model is then applied to a feedforward controller to enhance the tracking performance of the robot. The proposed modelling method first calculates the pose-dependent equivalent inertia of the system, then performs a few system identification experiments to determine the constant stiffness and damping coefficients, and then combines the two to predict the dynamics at any pose. The model is shown in experiments to accurately capture the pose-dependent vibration dynamics of the robot, and thus is effective for accurate tracking control.

However, the model has some inaccuracies due to unmodeled dynamics and nonlinearities. Future work will explore hybrid (i.e., physics-based and data-driven) modelling approaches, e.g., [19], to further improve the accuracy of the model and to automatically calibrate the model parameters if an unknown load is added. The proposed modelling and control methods will also be generalized in future work to include robotic arms with serial kinematics.

Declaration of competing interest

The authors declare the following financial interests/personal relationships which may be considered as potential competing interests: A company founded by Chinedum E. Okwudire holds a commercial license for the filtered B spline (FBS) algorithm. The FBS algorithm was used for tracking control in the submitted manuscript.

CRediT authorship contribution statement

Cheng-Hao Chou: Conceptualization, Data curation, Formal analysis, Investigation, Methodology, Software, Validation, Visualization, Writing – original draft, Writing – review & editing. **Chen Qian:** Conceptualization, Data curation, Investigation, Software, Validation. **Yung-Chun Lin:** Conceptualization, Methodology, Visualization, Writing – review & editing. **Shorya Awtar:** Conceptualization, Methodology, Funding acquisition. **Chinedum E. Okwudire:** Conceptualization, Funding acquisition, Methodology, Project administration, Supervision, Writing – review & editing.

Acknowledgements

This work is partially funded by the National Science Foundation grant # 2054715, and the Epicrew Corporation.

References

[1] Kaihara T, Kurose S, Fujii N (2012) A Proposal On Optimized Scheduling Methodology And Its Application To An Actual-Scale Semiconductor Manufacturing Problem. *CIRP Annals* 61(1):467–470.
[2] Lee HS, Jeong HD (2009) Chemical And Mechanical Balance In Polishing Of Electronic Materials For Defect-Free Surfaces. *CIRP Annals* 58(1):485–490.
[3] Yamamura K (2007) Fabrication of Ultra Precision Optics by Numerically Controlled Local Wet Etching. *CIRP Annals* 56(1):541–544.
[4] Jauregui Becker JM, Borst J, van der Veen A (2015) Improving The Overall Equipment Effectiveness In High-Mix-Low-Volume Manufacturing Environments. *CIRP Annals* 64(1):419–422.
[5] Mathia K (2010) *Robotics For Electronics Manufacturing*, Cambridge University Press.
[6] Reinhart G, Hoeppner J (2000) Non-Contact Handling Using High-Intensity Ultrasonics. *CIRP Annals* 49(1):5–8.
[7] Pritschow G (2000) Parallel Kinematic Machines (PKM) – Limitations and New Solutions. *CIRP Annals* 49(1):275–280.
[8] Merlet J-P (2000) *Parallel Robots*, SpringerNetherlands, Dordrecht.
[9] Higuchi T, Oka K, Sugawara H (1992) Clean Room Robot With Non-Contact Joints Using Magnetic Bearings. *Advanced Robotics* 7(2):105–119.
[10] Roth N, Schneider B (1993) Clean Room Industrial Robot for Handling and Assembly in Semiconductor Industry. *CIRP Annals* 42(1):21–24.
[11] Wang Z, Wang C, Tomizuka M (2015) Active Wide-Band Vibration Rejection for Semiconductor Manufacturing Robots. In: *Proceedings of the ASME 2015 Dynamic Systems and Control Conference*, .
[12] Altintas Y, Khoshdarregi MR (2012) Contour Error Control Of CNC Machine Tools With Vibration Avoidance. *CIRP Annals* 61(1):335–338.
[13] Yu X, Wang C, Zhao Y, Tomizuka M (2015) Controller Design And Optimal Tuning Of A Wafer Handling Robot. *2015 IEEE International Conference on Automation Science and Engineering (CASE)*, IEEE, , 640–646.
[14] Sencer B, Ishizaki K, Shamoto E (2015) High Speed Cornering Strategy With Confined Contour Error And Vibration Suppression For CNC Machine Tools. *CIRP Annals* 64(1):369–372.
[15] Okwudire C, Ramani K, Duan M (2016) A Trajectory Optimization Method For Improved Tracking Of Motion Commands Using CNC Machines That Experience Unwanted Vibration. *CIRP Annals* 65(1):373–376.
[16] Dumanli A, Sencer B (2019) Pre-compensation Of Servo Tracking Errors Through Data-Based Reference Trajectory Modification. *CIRP Annals* 68(1):397–400.
[17] Edoimioya N, Chou C-H, Okwudire CE (2023) Vibration Compensation Of Delta 3D Printer With Position-Varying Dynamics Using Filtered B-Splines. *The International Journal of Advanced Manufacturing Technology* 125(5):2851–2868.
[18] Yoon D, Okwudire CE (2015) Magnet Assisted Stage For Vibration And Heat Reduction In Wafer Scanning. *CIRP Annals* 64(1):381–384.
[19] Chou C-H, Duan M, Okwudire CE (2021) A Linear Hybrid Model For Enhanced Servo Error Pre-Compensation Of Feed Drives With Unmodeled Nonlinear Dynamics. *CIRP Annals* 70(1):301–304.